Journal of Materials Chemistry A

Accepted Manuscript

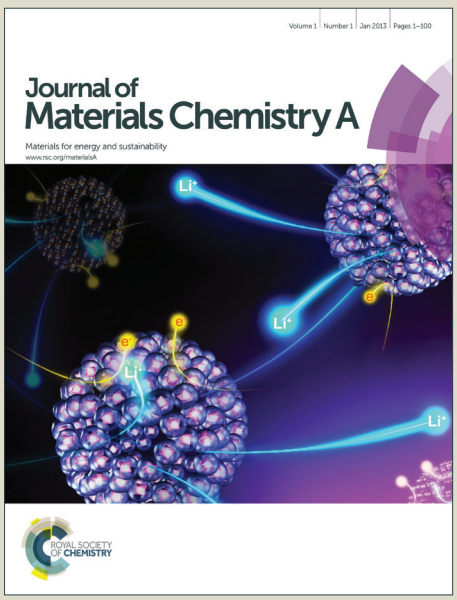

ROYAL SOCIETY OF CHEMISTRY

www.rsc.org/materialsA

A novel 3DOM TiO_2-carbon nancomposite is fabricated via a simple multicomponent infiltration of three-dimensionally ordered templates, and exhibits superior lithium ion storage performance.

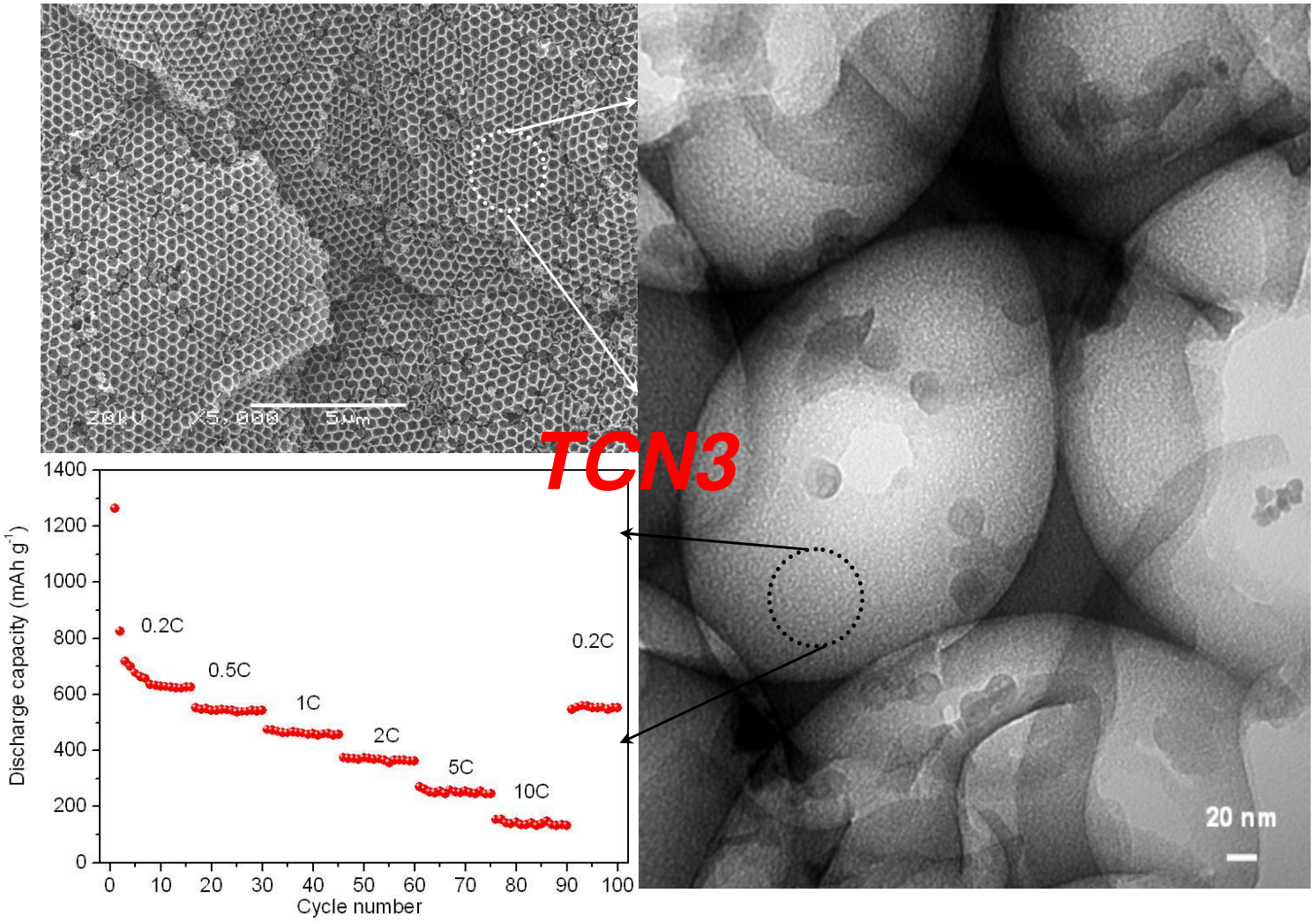

Facile synthesis of uniform constitution three-dimensionally ordered macroporous TiO_2-carbon nanocomposites with hierarchical pores for lithium ion batteries

Lihong Song,[ab] Ling Li,[b] Xin Gao,[ab] Jiaxin Zhao,[b] Ting Lu[b] and Zhi Liu *[ab]

[a]*Institute of Chemistry for Functionalized Materials, Faculty of Chemistry and Chemical Engineering, Liaoning Normal University, Dalian 116029, P. R. China*

[b]*Faculty of Chemistry and Chemical Engineering, Liaoning Normal University, Dalian 116029, P. R. China*

*Corresponding author. Tel.: +86 411 82156989; fax: +86 411 82156858.

E-mail address: zhiliu@lnnu.edu.cn

Abstract

In this work, we report several TiO_2-carbon nancomposites (TCNs) composing of homogeneous dispersion carbon and anatase TiO_2 nanocrystals (30.2-68.7wt.%) in a three-dimensionally ordered macroporous framework with pore-hierarchical structure fabricated by means of a simple multicomponent infiltration of three-dimensionally ordered templates. Galvanostatic charge/discharge and electrochemical impedance spectroscopy techniques are employed to assess the properties of these nanocomposites for use in lithium ion batteries. The results demonstrate that TiO_2 can be effectively utilized with assistance of the carbon in the electrode. The TCN3 (55.4 wt.% of TiO_2) is found to be the most efficient one with a high capacity of ~549 mAh g^{-1} at 0.2C after 100 cycles. In addition, it exhibits good cycling stability and superior rate capability as LIBs anode materials. The reversible capacity can still be remained at ~132 mAh g^{-1} at a high rate of 10C. Such TCN represents a promising exploring direction for enhancing the device performance of metal oxide-based electrode in lithium ion batteries.

1 Introduction

Since the pioneering discovery that titania (TiO_2) possessing a reversible lithium ion extraction/insertion behavior,[1] interests in TiO_2 as an anode material in lithium ion battery (LIB) have astonishingly increased over the past years. Compared with the conventional carbon-based anode materials, TiO_2 has a much higher operating voltage (~1.7 V versus Li/Li^+) and a lower cubical expansivity (3-4%). In addition, it is also chemically stable, abundant, inexpensive and environmentally benign. However, the poor abilities in lithium ion diffusivity and electronic conductivity (~10^{-12} S cm^{-1}) significantly lower its reversible capacity and high rate performance as an electrode material.[2, 3] There are two feasible strategies to overcome these drawbacks. One is to construct different TiO_2 polymorphs (TiO_2-B, rutile, anatase, or brookite) with morphology-controlled synthesis of various nanostructures, such as nanowires,[4, 5] nanotubes,[6, 7] nanosheets,[8] nanorods,[9] nanofibers,[10, 11] thin films,[12, 13] mesoporous nano-networks,[14, 15] *etc*. Although the nanocrystallization strategy can remarkably shorten the diffusion pathway for both electronic and lithium ion transport, increase the electrode/electrolyte contact area, and effectively enhance the durability against the strain of lithium ion insertion/extraction, it often results in TiO_2 nanocrystallines agglomeration with a low packing density. Furthermore, it is also possible that the TiO_2 nanocrystallines may detach from the electrode surface, cross the separator, and cause internal short circuits. The other alternative strategy is to hybridize the TiO_2 nanocrystallines with a second or even more phase materials, *i.e.*, fabricating TiO_2-based hybrids, including TiO_2-carbonaceous composites, TiO_2-P_2O_5 crystalline glass,[16] hydrogen titanate-TiO_2 nanowires,[17] binary or ternary composites of different types of heteroatoms or metal oxides with varied TiO_2

nanostructrures,[18-23] *etc*. Amongst the hybrid components, due to the low packing density, rich porosities for easy penetration of electrolyte, large surface area for charge transport, good electric conductivity, long cycle life, relatively low cost as well as versatile existing forms (porous carbons, graphene, carbon nanotubes, *etc*), carbonaceous materials are the most frequently used to prepare various TiO_2-carbonaceous composites with enhanced lithium storage capacities.[24-33]

In recent years, three-dimensionally ordered macroporous (3DOM) materials with uniform pore size and well-defined periodic structure have received much attention as hosts for lithium intercalation in LIBs research. 3DOM materials can make the electrolyte solution infiltrate the electrode easier if the pore sizes are in the range of several hundred nanometers. With the wall thickness only several tens of nanometers, 3DOM materials can reduce the diffusion distances of lithium ions significantly. As a continuous network of electrode materials, 3DOM materials are monolithic which have better electrical conductivity than nanocrystalline materials in which the particles are loosely aggregated together and should reduce the side reactions on high specific surface materials.[34, 35] Moreover, the ordered 3D frameworks are able to ensure much higher lithium ion flux across the electrode due to the dramatically increased electrode-electrolyte interface, and serve as the pathway for efficient electron transport. In addition, the free space within porous 3D electrodes can act as buffer for the volume variation of the entire electrode during the charge/discharge process.[36] Such merits of 3DOM materials in enhanced kinetics and electrode stability would potentially give rise to superior electrochemical performance in LIB. Traditionally, the colloidal crystal templating strategy (CCTS) is employed to prepare 3DOM materials.[37] Briefly, uniform monodispersed microspheres,

such as polystyrene (PS), silica or polymethyl methacrylate spheres, can assemble into ordered three-dimensional (3D) array in densified packing. These ordered arrays offer a 3D scaffold in which a variety of precursors can be infiltrated. After subsequent solidification of the precursor and removal of the colloidal spheres, periodic 3D framework structures are obtained. Moreover, more desired active species can be directly introduced into the 3DOM solid-state architecture through using the corresponding multi-component solution as precursor to infiltrate the template. This indicates that the possibility for obtaining a 3DOM composite material with uniform constitution. Based on these characteristics, various types of 3DOM materials, including $LiCoO_2$,[38] $Li_4Ti_5O_{12}$,[39, 40] $FePO_4$,[41] $LiMn_2O_4$,[42] Ni-Sn alloys,[43, 44] $Li_{1.5}Al_{0.5}Ti_{1.5}(PO_4)_3$,[45] $LiFePO_4$/C,[46] SnO_2,[47, 48] α-Fe_2O_3,[49] Ge,[50] FeF_3,[51] $Li_3V_2(PO_4)_3$/C,[52] and $CoFe_2O_4$,[53] *etc*, have been prepared and used as cathode or anode materials in LIBs successfully. In addition, Yang et al. prepared nano quasi-3DOM TiO_2 through in situ hydrolysis on poly(vinyl alcohol) gelated crystalline colloidal array photonic crystal films. As an anode material for LIBs, it exhibited a high rate capability and excellent cycle performance. The initial discharge/charge capacities were found to be 442 and 225 mA h g^{-1} at a current density of 25 mA g^{-1}, respectively.[54] More recently, Su et al. fabricated a 3DOM TiO_2 with disordered inter-particle mesopores and a 3DOMM TiO_2 with inner-particle mesopores by the CCTS and a surfactant-assisted CCTS, respectively. Both the 3DOM TiO_2 and the 3DOMM TiO_2 possessed excellent initial capacity of 248 mA h g^{-1} and 235 mA h g^{-1} at 0.2 C and 208 mA h g^{-1} and 202 mA h g^{-1} at 1C, respectively.[55] However, to the best of our knowledge, there were scarce reports on the synthesis of 3DOM TiO_2-carbon nanocomposite as an electrode material for LIB. Stein and Zhao et al. ever synthesized

3DOM TiO_2-carbon composites by a two-step method.[56, 57] For this method, 3DOM carbon was prepared with resorcinol-formaldehyde polymer or sucrose as carbon source via the CCTS in the first step. Then, the as-prepared 3DOM carbon was impregnated with different types of titanium sources in the second step. Unfortunately, in addition to the non-uniform titanium-carbon framework composition, as the increased reaction temperature or titanium source concentration, both of the resultants presented distinct macropores blockage, damage, even collapse of the 3DOM structure, which hindered their efficient utilization.

Inspired by the above elaboration, herein we first report the synthesis of a novel 3DOM TiO_2-carbon nanocomposite (TCN) by means of a multi-component (titanium sol, phenol-formaldehyde resol, and citric acid) infiltration of 3D templates. In this work, citric acid was selected as a good coordination agent to regulate the hydrolysis-polymerization of titanium species and resol. The resulting nanocomposite presents highly 3DOM structures, and the TiO_2 content in the nanocomposite can be continuously tuned from 30.2 to 68.7 wt.%. In contrast to previously reported TiO_2-carbonaceous composites, the walls of the present TCNs are composed of homogenously distributed TiO_2 and carbon. Moreover, the new nanocomposite is an excellent anode material for LIB, which exhibits superior electrochemical performance.

2. Experimental

2.1 Chemical reagents

Styrene and tetrabutoxytitanium (TBT) were purchased from Sigma-Aldrich. Phenol (P), formaldehyde (37 wt.%) (F), $K_2S_2O_8$, NaOH, and ethanol were purchased from chemical plants in China. All of the chemicals were used without further purification. Deionized

water was used in all experiments.

2.2 Synthesis of PS templates

The PS colloidal crystal templates for the preparation of TCN were synthesized via a soap-free-emulsion polymerization according to a procedure based on Ref. 58. In a typical synthesis, a desired amount of monomer styrene was washed four times with a NaOH solution (10wt.%) and di-distilled water respectively to remove any traces of the inhibitor. Then, 26.6 g of the washed styrene and 300 g of di-distilled water were added to a 500 mL round bottom flask and stirred for a while. Then, 15 mL (0.007g/mL) $K_2S_2O_8$ was added to the solution and the mixture was constantly reacted at 70 ^oC for 24h under a nitrogen atmosphere with mild stirring until a milky solution appeared. After filtering the milky solution to remove large agglomerates, the monodispersed PS microspheres were obtained. Finally, the as-synthesized monodispersed PS microspheres were packed into PS colloidal crystal template by evaporating the water solvent at 70 ^oC for 24 h.

2.3 Synthesis of precursors

The phenol-formaldehyde (PF) resol precursor was prepared according to Ref. 59. In a typical synthesis, 6.0 g of phenol was mixed with 1.0 g of 20 wt.% NaOH aqueous solution under stirring, and 10.0 g of formaldehyde solution was then added. The resulting transparent solution was stirred at 75 ^oC for 1 h, cooled to room temperature, and the pH was then adjusted to about 7.0 by 2.0 mol/L HCl. After water was removed by distillation, the mixture was redispersed in a required amount of ethanol. The NaCl precipitate was removed by filtration, and the filtrate, the PF resol precursor with a concentration of 50 wt.% in ethanol, was collected.

For a typical synthesis of titanium-PF precursor (TPP), a required amount of TBT and

1.00 g of citric acid were dissolved in 20 mL of ethanol under stirring for 30 min to form a transparent homogeneous solution. Afterwards, a desired amount of as-synthesized PF resol was added, and the mixture was further stirred overnight to obtain the TPP solution. By varying the amounts of TBT and PF resol, the TPPs with different carbon and titanium contents were prepared and denoted as TPP1, TPP2, TPP3, and TPP4, respectively. The detailed preparation conditions and the corresponding sample codes are summarized in Table 1.

2.4 Synthesis of TCNs

The TCNs were prepared by employing the CCTS with the different TPPs. Briefly, the as-synthesized PS templates were soaked in the TPP solution for 24 h. Care was taken to keep the solution level below the top of the PS template. After wiping off the excess solution and another 3h for the solvent evaporation under ambient conditions, the infiltered templates were transferred to a beaker and heated in an oven at 100 ^{o}C for 24 h to induce thermal polymerization. Then, the resultant was carbonized under flowing N_2 with a stepwise pyrolysis program as: 20 ^{o}C $\xrightarrow{430\,min}$ 450 ^{o}C $\xrightarrow{180\,min}$ 450 ^{o}C $\xrightarrow{350\,min}$ 800 ^{o}C $\xrightarrow{120\,min}$ 800 ^{o}C. After pyrolysis, the color of the samples became from pale yellow to completely black. The final products were denoted as TCN1, TCN2, TCN3, and TCN4, respectively. The thermogravimetric analysis results showed that the weight loss of TCN1, TCN2, TCN3, and TCN4 were 69.8 wt.%, 54.7 wt.%, 44.6 wt.% and 31.3 wt.%, respectively. The corresponding TiO_2 weight contents in the TCNs were converted to 30.2 wt.%, 45.3 wt.%, 55.4 wt.%, and 68.7 wt.% accordingly.

2.5 Characterizations

Thermogravimetric analysis (TG) was performed with a Diamond Pyris

thermogravimetric analyzer at a ramping rate of 10 ^{o}C/min in an air flow of 100 mL/min. Scanning electron microscopy (SEM) images were obtained with a JSM6360-LV microscope. The samples were vapor-deposited with gold before observation. Transmission electron microscopy (TEM) image were obtained on a JEOL 2010 electron microscope at 200 kV. Prior to the observation, the samples were ultrasonically dispersed in ethanol and then dropped onto carbon-coated copper grids. Powder X-ray diffraction (XRD) pattern was collected with a Rigaku D/Max-βb diffractometer using a Cu Kα radiation source (λ=0.15432 nm). Wide-angle diffractions were recorded at a scanning speed of 5^{o} min^{-1}. Textural characterization was carried out by N_2-sorption at -196 ^{o}C on a Micromeritics ASAP 2010 apparatus. Prior to the measurements, the samples were degassed at 200 °C for 3 h. The Brunauer-Emmett-Teller (BET) method was used to calculate the specific surface areas (S_{BET}). The pore size distribution (PSD) and the mesopore volume (V_{mes}) were derived from the adsorption branches of the isotherms using the Barrett-Joyner-Halenda (BJH) method. The total pore volume (V_p) was estimated from the adsorption branches at a relative pressure (P/P_0) of 0.998. The micropore volume (V_{mic}) was determined according to the *t*-plot method. X-ray photoelectron spectroscopy (XPS) was conducted on a PHI 5700 ESCA spectrometer with amonochromated Al Ka radiation source. Spectra correction was conducted using the C 1s line at 284.6 eV.

2.6 Electrochemical measurements

The electrochemical measurements were carried out using standard CR 2025 type coin cells.. The as-synthesized TCNs were mixed with polyvinylidene fluoride (binder) and acetylene black carbon (conducting agent) in a weight ratio of 80:10:10. Lithium foil was

used as both the counter and the reference electrodes. The electrolyte was 1 M solution of $LiPF_6$ in a 50:50 (w/w) mixture of ethylene carbonate and diethyl carbonate. Celgard 3400 membrane was employed as a separator. Test cells were assembled in an argon-filled glove box, where water and oxygen concentrations were kept less than 1 ppm. Galvanostatic charge/discharge (GCD) tests were conducted using a battery tester LAND-CT2001A with a voltage window of 1-3 V under ambient temperature at different current rates where 1C = 170 mA g^{-1}. Electrochemical impedance spectroscopy (EIS) measurements were carried out by applying an alternating current of 5 mV in the frequency range from 100 kHz to 10 mHz.

3 Results and discussion

3.1 Characteristics of TCNs

The uniformity of the templates was confirmed from SEM observation. Fig. 1a illustrates the typical SEM image of the colloidal crystal templates assembled by PS microspheres with an average diameter of 460 nm. It could be seen that the template was perfectly uniform and orderly with long range in a large area. A hexagonal close-packed arrangement of PS microspheres, where each microsphere was connected with its nearest six neighbors in the same layer, was observed. When the as-synthesized TPP solutions were infiltrated into the interstices of the PS templates arrays, the solutions could penetrate into the voids by capillary force. After drying out, they formed 3D skeleton in the templates, and TCNs were finally achieved after removing the templates by pyrolysis. Fig. 1b-1e depicts the SEM images of the resulting TCNs. It was clearly observed that the TCN1, TCN2, and TCN3 exhibited the interconnected networks of ordered macropore structures with a pore size of 250-400 nm suggesting significant shrinkage of the PS

templates occurring during pyrolysis. However, the quality of 3DOM structure differed from sample to sample. For the TCN1 obtained with high weight rate of PF resol to TBT (P/T) of 3.88, the 3DOM structure was frail and fractured (Fig. 1b). Incomplete infiltration of the TPP solution into the PS templates caused distinct pores blockage of next layer. This was stemmed from the fast PF polymerization accompanying with the overwhelming growth of the cross-linked PF monomer. As a result, major of PS microspheres were covered and pores blockage appeared after the following pyrolysis treatment. After the P/T was lessened to 2.29, the 3DOM alignment of the TCN2 was relatively uniform with scattered pores blockage and breakage as the circular rings shown (Fig. 1c). As the P/T was further lessened to 1.51, the TCN3 presented an intact and solid three-dimensional ordered arrangement of interconnected macroporous framework with an average macropore diameter of 320 nm (Fig. 1d). When the P/T was finally lessened to 0.95, there were scarcely any discernible 3DOM skeletons in the TCN4 except for a rambling and incompact particle arrangement (Fig. 1e), presumedly arising from the decrease of mechanical strength in skeleton caused by the decrease of carbon content. The great discrepancy in morphology for the TCNs was probably due to the difference of P/T, which led to form varied TPP solutions with different TBT hydrolyzing and PF resol polymerizing rates in the presence of citric acid. Only when the hydrolyzing-polymerizing rate was adjusted to an optimum steady-state, would it give rise to an appropriate TPP solution to facilitate the filling the voids in the template via a steady fluid-solid transformation.[60, 61] As a result, the desired 3DOM structure of TCN would be constructed perfectly.

Fig. 2 records the wide-angle XRD patterns of the TCNs. One can only observe two

broad peaks at 23° and 42° which were typical of amorphous carbon materials.[62, 63] No reflections corresponding to crystalline titania phases were observed, indicating that the titania species in the nanocomposites were either amorphous or highly dispersed in the framework. To further check if the titanium and carbon were homogeneously dispersed in the walls of the TCNs, we performed energy-dispersive X-ray analysis on the TCN3 in an elemental mapping mode. It was seen in Fig. 1f that the carbon spectrum was totally consistent with the titanium spectrum, confirming that the walls were composed of homogeneously dispersed carbon and titanium species in interpenetrating form.

Figure 3 presents the nitrogen adsorption-desorption isotherm as well as the corresponding PSDs of the TCNs. All the samples exhibited representative type II isotherms with combination forms of a distinct H2 type hysteresis loop in the P/P_0 range of 0.2-0.8 and a well-defined H3 hysteresis loop in the P/P_0 range of 0.8-1.0. The type H2 hysteresis loop is often associated with capillary condensation of the mesopores, indicating the existence of mesopores within the wall structure. The type H3 hysteresis loop, characteristic of lacking a clear adsorption plateau at $P/P_0 \approx 1.0$, is usually as a signal for a macropore size distribution tendency. Both the isotherms and the hysteresis loops of the four samples were very similar to those of the reported three-dimensionally ordered macro-mesoporous materials.[64-72] In addition, it should be point out that below the very low relative pressure of $P/P_0 = 0.1$, there was a significant quick rise of adsorption branch, indicating the presence of considerable micropores generated from the carbonization of PF resol. It could therefore be inferred that the present TCNs contained macropores together with the meso- and micropores. Amongst the samples, the TCN2 and TCN3 exhibited much more clearly observable type H2 hysteresis loops, indicating

the generation of much better mesoporous architecture from the PSDs. Each of the samples showed a rather narrow PSD centered at about 4.1-4.8 nm and a broad PSD that was scattered from 30 to 110 nm. In addition, it deserves to be mentioned that the peak intensity of the PSD for the TCN1 and TCN4 centered at 4.1-4.8 nm decreased stringkingly, indicating that the relatively low proportion of mesopores in the two samples. Table 2 lists the textural properties of the TCNs. Amongst the TCNs, the TCN3 possessed the largest S_{BET} of 655 m^2 g^{-1} and highest V_p of 0.57 cm^3 g^{-1}. Its V_{mes} and V_{mic} were 0.43 and 0.13 cm^3 g^{-1}, respectively, indicating that substantial mesopores were present in the sample. The other three samples had relatively lower V_{mes} accompanying with varied V_{mic} from 0.06 to 0.15 cm^3 g^{-1}, suggesting that the variation of content of the constitutive titanium and carbon sources in TPPs could exert a great impact on the amounts of mesopore and micropore in TCN. This was possibly assigned to the effect of the polymerization and carbonization processes catalyzed by the differing metal ions. Similar phenomena have also been reported by Moreno-Castilla et al.[73]

Fig. 4 illustrates the representative TEM image of the TCN3 at different magnification. It was clearly observed in Fig. 4a that the sample exhibited a high-quality 3DOM structure with the macropore size of around 250 nm, in accordance with its SEM observation. The partial magnified image in Fig. 4b showed that the 3DOM skeleton was composed of uniform constitution, and no bulk aggregates of TiO_2 were found on the 3DOM carbon scaffold. In the high-resolution TEM image (Fig. 4c), the crystal lattice fringes with *d*-spacing of 0.35 nm corresponding to the (101) plane of the anatase TiO_2, can be clearly observed, whereas no significant crystalline plane of carbon was found, implying its amorphous nature. These were well consistent with the XRD results. In

addition, there were numerous mesopores with sizes in the range of 3-5 nm randomly distributed in the macropore walls of the 3DOM carbon scaffold, coinciding with the PSD analysis. The emergence of mesopores contributed the enhancement in surface area. It was commonly recognized that electrochemical performances could be significantly improved by increasing the surface area of the anode materials. Hence, the TCN in our case will potentially afford much more accessible interior or exterior surface sites for electrode/electrolyte contact areas and interface lithiation.[74]

XPS is a useful technique to investigate the element composition and metal oxidation states. Because of the indeterminate valence of titanium species from the XRD patterns, we conducted XPS to further probe the chemical state of titanium atoms in the TCNs. Fig. 5 shows the Ti 2*p* XPS spectra of the TCNs. There were two symmetric Ti 2*p* peaks located at around 458.6 and 464.4 eV, respectively, which were attributed to the binding energies of Ti $2p_{3/2}$ and $2p_{1/2}$ and in good agreement with the results expected for the Ti^{4+} oxidation state.[75] Exceptionally somewhat, the spin-energy separation (ΔE) between these two peaks was 5.8 eV, slightly larger than the ΔE value (5.5 eV) reported for TiO_2. This was presumedly attributed to the existence of some Ti-O-C on the TiO_2/carbon interface.[76, 77] In addition, there was an obvious increase in the Ti 2*p* intensity correlating well with the increasing TiO_2 content from TCN1 to TCN4.

3.2 Electrochemical performance

The present TCNs containing 3DOM network with a hierarchically porous structure and uniform composition provides a promising electrode material for enhancing performance of TiO_2-based LIBs. The electrochemical performances of the TCNs in the LIB were examined by GCD tests. Fig. 6 reveals the GCD voltage profiles of the TCNs at a current

rate of 0.2C. For the TCN1 (Fig. 6a), TCN2 (Fig. 6b), TCN3 (Fig. 6c), and TCN4 (Fig. 6d), the typical voltage plateaus for discharging (1.7-1.8 V) and charging (1.9-2.0 V) processes of anatase TiO_2, reflecting the dominant lithium-ion insertion/deinsertion processes between the tetragonal and orthorhombic phases with lithiated reaction into anatase TiO_2, were not found.[16, 26, 78] This was probably due to the high carbon content in the four samples (31.3-69.8 wt.%). The TCN3 showed the largest first discharge and charge capacities (~1263 and ~709 mAh g^{-1}) in the four samples, corresponding to a coulombic efficiency of 56%. The large capacity loss was mainly attributed to the formation of a solid electrolyte interphase (SEI) layer on the electrode surface during the first discharge [79] and the high specific surface area of the porous carbon in the TCN3, which consumed a much higher amount of irreversible lithium ions to form the SEI layer.

In order to further understand the GCD results, EIS was used to quantify the conductive and diffusive behavior of the TCN electrodes. Fig. 7 records Nyquist plots of the TCN electrodes with different TiO_2 contents. It was noted that all of the electrodes had a comparable ohmic resistance with a single semicircle in the high frequency region and a sloping line in the low frequency region. The diameter of the high-frequency semicircle corresponded to the charge-transfer resistance (R_{ct}) at electrolyte/electrode interface. And the sloping line at low frequency reflected the diffusion resistance (Warburg resistance, Z_w) of lithium ions on electrode.[80] The larger of the Z_w, the lower sloping line slop. The R_{ct} fitting values of the TCNs were 45.7, 37.2, 22.8, and 72.6 Ω for the TCN1, TCN2, TCN3, and TCN4, respectively. Apparently, the more intact and solid 3DOM framework of the TCN3 did afford much more effective conductive pathways, dramatically reducing the contact and charge-transfer resistance, compared with the

TCN1, TCN2, and TCN4. On the other hand, with the increasing TiO_2 content, the slope of the Nyquist plot in the low frequency region followed the order, TCN1 > TCN2 ≈ TCN3 > TCN4, indicating that higher TiO_2 content led to larger Z_w. Therefore, in order to achieve good capacitance performance for the TCN electrodes, it is crucial to maintain a connective carbon framework with good conductivity and introduce a rational TiO_2 content.

Fig. 8 shows the capacity *versus* cycle number curves from the first cycle to the 100th cycle of the TCN electrodes between 1 and 3 V at a current density of 0.2C. It was noted that the TCN3 electrode possessed the most stable cycling performance and a higher reversible capacity of approximately 549 mAh g^{-1} up to 100 cycles, with a high coulombic efficiency of ~98%. In our CCTS synthesis procedure, the titanium source (TBT) had been homogeneously mixed with the carbon source (PF resol) before they were subjected to template infiltration and pyrolysis, which would consequentially produce strong interaction with the surrounding carbon during the pyrolysis. Thus, the carbon would significantly inhibit the TiO_2 nanocrystallines agglomeration and growth. As a result, drastic TiO_2 volume variation would not arise during the lithium insertion/extraction process, and stable cycling performance can be well remained. Comparatively, the reversible capacities of TCN1, TCN2, and TCN4 after 100 cycles were 381, 481, and 356 mAh g^{-1} respectively with obvious decay trends. The coulombic efficiencies, ~76% for TCN1, ~91% for TCN2 and ~82% for TCN4, were also lower than that of TCN3. The low reversible capacities were primarily originated from the relatively low S_{BET}, V_p, and little proportion of mesopores in the three samples (Table 2 and Fig. 3). In addition, the excess carbon or TiO_2 content with intrinsically high lithium-ion

insertion/deinsertion or diffusion resistance might be another disadvantage for the capacity deterioration of the three samples.

In order to better understand the rate performance of the TCN, TCN3, the most efficient electrode, was selected to investigate the cycling response at continuously variable rates. For comparison, the rate capability testing measurements were also performed on pure 3DOM TiO_2 nanocrystals (Fig. S1) and 3DOM carbon (Fig. S2) synthesized by the same CCTS with single TBT-citric acid solution or PF resol as the precursor. As shown in Fig. 9a, the TCN3 exhibited a high discharge capacity of ~625 mAh g^{-1} at the current density of 0.2C after 15 cycles. This value lessened to ~542 mAh g^{-1} at the current density of 0.5C, ~457 mAh g^{-1} at the current density of 1C, and ~363 mAh g^{-1} at the current density of 2C. Even at the higher current densities of 5C and 10C, the discharge capacities of the TCN3 kept at steady values of ~247 and ~132 mAh g^{-1}, respectively (Fig. 8b). The discharge capacity was recovered to ~551 mAh g^{-1} when the current rate was restored to 0.2C. After 100 cycles, the 3DOM structure of the TCN3 was still well-maintained with partial pore damage to some extent, and the whole structural integrity remained considerably, as shown in Fig. 9b, implying that the long-term charge/discharge cycles did not severely spoil the structure of the TCN3 and the high discharge capacity could be further well preserved. In contrast, the rate capabilities of the 3DOM TiO_2 nanocrystals and 3DOM carbon showed inferior performances, and the discharge capacity decreased drastically from ~186 and ~145 mAh g^{-1} at 0.2C to ~33 and ~15 mAh g^{-1} at 10C, respectively (Fig. S3 and S4). Recently, Liu et al. prepared a 3D disorder TiO_2/carbon co-aerogel (58.2 wt.% of TiO_2 with an S_{BET} of 478 m^2 g^{-1} and a R_{ct} of > 100 Ω) by a one-pot process with titanium isopropoxide and

resorcinole-formaldehyde resol as precursors and investigated their capacitive performance in LIB. The reversible discharge capacity of the co-aerogel was stabilized at ~400 mAh g^{-1} at a current density of 1C. They ascribed the superior lithium storage capability to high uniformity of composites, small TiO_2 size, stable mechanical strength, and low internal resistance.[81] In our case, the TCN3 exhibited a higher reversible capacity of ~457 mAh g^{-1} than the TiO_2/carbon co-aerogel at the same current density of 1C. Considering the similar TiO_2 content (55.4 wt.% of TiO_2) and uniform TiO_2-carbon constitution as the TiO_2/carbon co-aerogel, the highly 3DOM structure with a richer porosity (S_{BET} of 655 m^2 g^{-1}) and a much lower R_{ct} (22.8 Ω) of the TCN3 was supposed to be the crucial factor for the enhancement of reversible capacity. In addition, we compared the capacitive performance of the TCN3 with other TiO_2-based composite electrodes reported previously, as tabulated in Table 3. Clearly, our capacities were higher than or comparable to those of reported data under the same condition with less TiO_2 usage.[54, 55, 24-27, 33, 82-84, 29, 85, 86] These performances, on the other hand, also outperformed those of some reported Ti-based multimetallic oxide porous anode materials, such as 3DOM $Li_4Ti_5O_{12}$, mesoporous $Li_4Ti_5O_{12}$/C nanocomposite, ordered mesoporous $TiNb_2O_7$, and C-$TiNb_2O_7$ composite (Table S1), further verifying the superior lithium-ion insertion/extraction performance of the TCN3.

The excellent electrochemical performance of the TCN3 electrode was mainly attributed to its special architecture. As demonstrated in Fig. 10, the TCN3 was hierarchically porous structure. There were numerous mesopores and micropores in the macropore walls of the well-developed interconnected 3DOM TCN3 framework. Moreover, titanium and carbon were homogenously dispersed in the macropore walls

where more lithium ions could be smoothly intercalated into the lattices of carbon and anatase TiO_2 and react with them. These features were favorable to shorten the diffusion length for both electrons and lithium ions, improve the electronic conductivity, prevent the TiO_2 aggregation and growth during cycling, and increase the accessible internal surface area to penetrate much more electrolyte for a higher interfacial charge transfer. In addition, the large hollow interior of the TCN3 could act as an electrolyte reservoir, which was conductive to store much more electrolyte and lead to a higher lithium-ion flux across the interface. In the present voltage range, the mechanism involved in the reaction between lithium ions and TCN3 can be described by the following two reactions:

$$6C + xLi^+ + xe^- \longleftrightarrow Li_xC_6$$

$$TiO_2 + yLi^+ + ye^- \longleftrightarrow Li_yTiO_2$$

where x represents a stoichiometric factor in Li_xC_6, and y indicates the insertion coefficient of Li_yTiO_2. Generally x is ~1.0 for graphitic carbon, 0.5-0.8 for low-capacity non-graphitic carbon, and 1.2-3.0 for high-capacity non-graphitic carbon, while y is usually close to 1.0 for anatase TiO_2. During the first several charge/discharge cycles, the contribution from lithium ion intercalation to carbon of TCN3 can be identified because of the high irreversible capacity and relatively low intercalation potential. During the subsequent charge/discharge cycles, the capacity should mainly come from the intercalation/deintercalation of lithium ion into anatase TiO_2.

4 Conclusions

We have successfully prepared the 3DOM TCNs *via* a simple multi-component infiltration of 3D PS templates followed by a direct pyrolysis process. The integration of carbon and TiO_2 in 3DOM architecture enables such a nanocomposite to possess

homogeneous dispersion and strong interaction between the two components. As an electrode material in LIB, the TCN3 was the most efficient one which displayed the highest reversible capacity, best cycability, and most excellent rate capability in the current density range of 0.2-10C. Such superior electrochemical behavior can be attributed to the hierarchical structure of the TCN and positive synergetic contributions of carbon and TiO_2, which creates a series of enhancements in function, including short diffusion length for both electrons and lithium ions, large accessible surface area, homogeneously dispersed TiO_2, and the enhanced lithium-ion flux. These results should deepen the understanding of the role of combining hierarchical ordered macrostructure with TiO_2 in electrochemical application. Moreover, this work conceptually provides a way for tailoring/designing 3DOM metal (oxide)-carbon nanocomposites to many different electrode materials for advanced energy storage and conversion devices, and thus is worthy of further exploration.

Acknowledgements

This work was financially supported by the National Natural Science Foundation of China (No.21071072) and the Doctoral Program Foundation of Liaoning Province (No. 20091047). We also thank Mr. Gang Zhao (College of Environmental Science and Engineering, Dalian Maritime University) for running XPS measurements.

Notes and references

1 T. Ohzuku, Z. Takehara and S. Yoshizawa, *Electrochim. Acta*, 1979, **24,** 219.

2 T. Fröschl, U. Hörmann, P. Kubiak, G. Kučerová, M. Pfanzelt, C. K. Weiss, R. J. Behm, N. Hüsing, U. Kaiser, K. Landfester and M. Wohlfahrt-Mehrens, *Chem. Soc. Rev.*, 2012, **41**, 5313.

3 H. B. Wu, J. S. Chen, H. H. Hng and X. W. (David) Lou, *Nanoscale*, 2012, **4**, 2526.

4 J. M. Li, W. Wan, H. H. Zhou, J. J. Li and D. S. Xu, *Chem. Commun.*, 2011, **47**, 3439.

5 F. X. Wu, X. H. Li, Z. X. Wang, H. J. Guo, L. Wu, X. H. Xiong and X. J. Wang, *J. Alloy. Compd.*, 2011, **509**, 3711.

6 H. Q. Li, S. K. Martha, R. R. Unocic, H. M. Luo, S. Dai and J. Qu, *J. Power Sources*, 2012, **218**, 88.

7 H. Han, T. Song, E. K. Lee, A. Devadoss, Y. Jeon, J. Ha, Y. C. Chung, Y. M. Choi, Y. G. Jung and U. Paik, *ACS Nano*, 2012, **6**, 8308.

8 J. S. Chen and X. W. (David) Lou, *Mater. Today*, 2012, **15**, 246.

9 T. Tao, and Y. Chen, *Mater. Lett.*, 2013, **98**, 112.

10 W. Luo, X. L. Hu, Y. M. Sun and Y. H. Huang, *J. Mater. Chem.*, 2012, **22**, 4910.

11 R. Qing, L. Liu, C. Bohling and W. Sigmund, *J. Power Sources*, 2015, **274**, 667.

12 M. J. Wang, C. F. Li, W. J. Lai and S. K. Yen, *Thin Solid Films*, 2012, **520**, 6744.

13 J. Mani, H. Katzke, S. Habouti, K. R. Moonoosawmy, M. Dietze and M. Es-Souni, *J. Mater. Chem.*, 2012, **22**, 6632.

14 K. Saravanan, K. Ananthanarayanan and P. Balaya, *Energy Environ. Sci.*, 2010, **3**, 939.

15 Y. Ma, G. Ji, B. Ding and J. Y. Lee, *J. Mater. Chem.*, 2012, **22**, 24380.

16 Y. G. Wang, H. Q. Li, P. He, E. Hosono and H. S. Zhou, *Nanoscale*, 2010, **2**, 1294.

17 F. X. Wu, Z. X. Wang, X. H. Li and H. J. Guo, *J. Mater. Chem.*, 2011, **21**, 12675.

18 S. M. Paek, J. H. Kang, H. Jung, S. J. Hwang and J. H. Choy, *Chem. Commun.*, 2009, 7536.

19 Z. Ali, S. N. Cha, J. I. Sohn, I. Shakir, C. Z. Yan, J. M. Kim and D. J. Kang, *J. Mater. Chem.*, 2012, **22**, 17625.

20 X. Zhang, P. S. Kumar, V. Aravindan, H. H. Liu, J. Sundaramurthy, S. G. Mhaisalkar, H. M. Duong, S. Ramakrishna and S. Madhavi, *J. Phys. Chem. C*, 2012, **116**,14780.

21 M. Tian, W. Wang, Y. Liu, K. L.Jungjohann, C. T. Harris, Y. C. Lee, R. G. Yang, *Nano Energy*, 2015, **11**, 500.

22 J. X. Qiu, P. Zhang, M. Ling, S. Li, P. R. Liu, H. J. Zhao and S. Q. Zhang, *ACS Appl. Mater. Interfaces*, 2012, **4**, 3636.

23 P. Zhang, J. X. Qiu, Z. F. Zheng, G. Liu, M. Ling, W. Martens, H. H. Wang, H. J. Zhao, S. Q. Zhang, *Electrochim. Acta*, 2013, **104**, 41.

24 J. S. Chen, H. Liu, S. Z. Qiao and X. W. (David) Lou, *J. Mater. Chem.*, 2011, 21, 5687.

25 F. F. Cao, X. L. Wu, S. Xin, Y. G. Guo and L. J. Wan, *J. Phys. Chem. C*, 2010, **114**, 10308.

26 S. K. Das, S. Darmakolla and A. J. Bhattacharyya, *J. Mater. Chem.*, 2010, **20**, 1600.

27 B. T. Zhao, R. Cai, S. M. Jiang, Y. J. Sha and Z. P. Shao, *Electrochim. Acta*, 2012, **85**, 636.

28 P. C. Chen, M. C. Tsai, H. C. Chen, I. N. Lin, H. S. Sheu, Y. S. Lin, J. G. Duh, H. T. Chiu and C. Y. Lee, *J. Mater. Chem.*, 2012, **22**, 5349.

29 P. Y. Chang, C. H. Huang and R. A. Doong, *Carbon*, 2012, **50**, 4259.

30 J. W. Xu, Y. F. Wang, Z. H. Li and W. F. Zhang, *J. Power Sources*, 2008, **175**, 903.

31 F. F. Cao, Y. G. Guo, S. F. Zheng, X. L. Wu, L. Y. Jiang, R. R. Bi, L. J. Wan and J. Maier, *Chem. Mater.*, 2010, **22**, 1908.

32 D. H. Wang, D. W. Choi, J. Li, Z. G. Yang, Z. M. Nie, R. Kou, D. H. Hu, C. M. Wang, L. V. Saraf, J. G. Zhang, I. A. Aksay and J. Liu, *ACS Nano*, 2009, **3**, 907.

33 L. F. He, R. G. Ma, N. Du, J. G. Ren, T. L. Wong, Y. Y. Li and S. T. Lee, J. *Mater. Chem.*, 2012, **22**, 19061.

34 F. Y. Cheng, Z. L. Tao, J. Liang and J. Chen, *Chem. Mater.*, 2008, **20**, 667.

35 K. T. Lee and J. Cho, *Nano Today* 2011, **6**, 28.

36 L. Yu, Z. Y. Wang, L. Zhang, H. B. Wu and X. W. (David) Lou, *J. Mater. Chem. A*, 2013, **1**, 122.

37 M. A. Al-Daous and A. Stein, *Chem. Mater.*, 2003, **15**, 2638.

38 J. J. Peng, T. J. Zhang, H. M. Zhang, Z. Y. Zhang, Z. H. Li and G. T. Lei, *J. Solid State Electrochem.*, 2012, **16**, 3079.

39 E. M. Sorensen, S. J. Barry, H. K. Jung, J. R. Rondinelli, J. T. Vaughey and K. R. Poeppelmeier, *Chem. Mater.*, 2006, **18**, 482.

40 S. W. Woo, K. Dokko and K. Kanamur, *Electrochim. Acta*, 2007, **53**, 79.

41 W. J. Cui, H. J. Liu, C. X. Wang and Y. Y. Xia, *Electrochem. Commun.*, 2008, **10** 1587.

42 D. Tonti, M. J. Torralvo, E. Enciso, I. Sobrados and J. Sanz, *Chem. Mater.*, 2008, **20**, 4783-4790.

43 K. Nishikawa, K. Dokko, K. Kinoshita, S. W. Woo and K. Kanamura, *J. Power Sources*, 2009, **189**, 726.

44 S. W. Woo, N. Okada, M. Kotobuki, K. Sasajima, H. Munakata, K. Kajihara and K. Kanamura, *Electrochim. Acta*, 2010, **55**, 8030.

45 M. Kotobuki, Y. Isshiki, H. Munakata and K. Kanamura, *Electrochim. Acta*, 2010, **55**,

6892.

46 A. Vu and A. Stein, *Chem. Mater.*, 2011, **23**, 3237.

47 J. C. Lytle, H. W. Yan, N. S. Ergang, W. H. Smyrl and A. Stein, *J. Mater. Chem.*, 2004, **14**, 1616.

48 C. H. Yim, E. A. Baranova, F. M. Courtel, Y. A. Lebdeh and I. J. Davidson, *J. Power Sources*, 2011, **196**, 9731.

49 Z. Liu, J. H. Mia Y. Yang, J. Li and X. L. Tan, *Mater. Sci. Eng. B*, 2012, **177**, 1612.

50 X. Liu, J. P. Zhao, J. Hao, B. L. Su and Y. Li, *J. Mater. Chem. A*, 2013, **1**, 15076.

51 D. L. Ma, Z. Y. Cao, H. G. Wang, X. L. Huang, L. M. Wang and X. B. Zhang, *Energy Environ. Sci.*, 2012, **5**, 8538.

52 D. L. Li, M. Tian, R. Xie, Q. Li, X. Y. Fan, L. Gou, P. Zhao, S. L. Ma, Y. X. Shi and H. T. H. Yong, *Nanoscale*, 2014, **6**, 3302.

53 Z. H. Li, T. P. Zhao, X. Y. Zhan, D. S. Gao, Q. Z. Xiao and G. T. Lei, *Electrochim. Acta*, 2010, **55**, 4594.

54 H. L. Jiang, X. L. Yang, C. Chen, Y. H. Zhu and C. Z. Li, *New J. Chem.*, 2013, **37**, 1578-1583.

55 J. Jin, S. Z. Huang, J. Liu, Y. Li, D. S. Chen, H. E. Wang, Y. Yu, L. H. Chen and B. L. Su, *J. Mater. Chem. A*, 2014, **2**, 9699.

56 Z. Y. Wang, N. S. Ergang, M. A. Al-Daous and Andreas Stein, *Chem. Mater.*, 2005, **17**, 6805.

57 S. Li, D. F. Zhao, J. T. Zheng, Y. Wan, X. S. Zhao, C. C. Zhao, Y. Liu, F. Liu, L. Lu and Y. Q. Wang, *Mater. Res. Bull.*, 2010, **45**, 1069.

58 Z. Liu, Y. Yang, J. H. Mi, X. L. Tan and C. Lv, *Int. J. Hydrogen Energy*, 2013, **38**,

4445.

59 Y. Meng, D. Gu, F. Q. Zhang, Y. F. Shi, H. F. Yang, Z. Li, C. Z. Yu, B. Tu and D. Y. Zhao, *Angew. Chem. Int. Ed.*, 2005, **44**, 7053.

60 H. W. Yan, C. F. Blanford, B. T. Holland, W. H. Smyrl and A. Stein, *Chem. Mater.*, 1999, **11**, 795.

61 H. W. Yan, C. F. Blanford, B. T. Holland, W. H. Smyrl and A. Stein, *Chem. Mater.*, 2000, **12**, 1134.

62 Z. Liu, A. Q. Wang, X. D. Wang and T. Zhang, *Catal. Today*, 2008, **137**, 162.

63 Z. Liu, Y. Yang, J. H. Mi, X. L. Tan, Y. Song, *Catal. Commun.*, 2012, **21**, 58.

64 R. Z. Zhang, H. X. Dai, Y. C. Du, L. Zhang, J. G. Deng, Y. S. Xia, Z. X. Zhao, X. Meng and Y. X. Liu, *Inorg. Chem.*, 2011, **50**, 2534.

65 H. Zhang, H. X. Dai, Y. X. Liu, J. G. Deng, L. Zhang and K. M. Ji, *Mater. Chem. Phys.*, 2011, **129**, 586.

66 J. Q. Zhao, P. Wan, J. Xiang, T. Tong, L. Dong, Z. N. Gao, X. Y. Shen and H. Tong, *Microporous Mesoporous Mater.*, 2011, **138**, 200.

67 Y. X. Liu, H. X. Dai, Y. C. Du, J. G. Deng, L. Zhang, Z. X. Zhao and C. T. Au, *J. Catal.*, 2012, **287**, 149.

68 Z. X. Zhao, H. X. Dai, J. G. Deng, Y. C. Du, Y. X. Liu and L. Zhang, *Microporous Mesoporous Mater.*, 2012, **163**, 131.

69 D. Z. Han, X. Li, L. Zhang, Y. H. Wang, Z. F. Yan and S. M. Liu, *Microporous Mesoporous Mater.*, 2012, **158**, 1.

70 H. Arandiyan, H. X. Dai, J. G. Deng, Y. X. Liu, B. Y. Bai, Y. Wang, X. W. Li, S. H. Xie and J. H. Li, *J. Catal.*, 2013, **307**, 327.

71 Y. C. Wei, Z. Zhao, T. Li, J. Liu, A. J. Duan and G. Y. Jiang, *Appl. Catal. B*, 2014, **146**, 57.

72 Z. Liu, X. L. Tan, X. Gao and L. H. Song, *J. Power Sources*, 2014, **267**, 812.

73 F. J. Maldonado-Hódar, M. A. Ferro-García, J. Rivera-Utrilla and C. Moreno-Castilla, *Carbon*, 1999, **37**, 1199.

74 J. Z. Chen, L. Yang and Y. F. Tang, *J. Power Sources*, 2010, **195**, 6893.

75 D. Briggs and J. C. Riviere, *Practical Surface Analysis by Auger and X-ray Photoelectron Spectroscopy*, ed. D. Briggs and M. P. Seah, John Wiley & Sons, London, 1983, pp. 87-139.

76 S. B. Amor, G. Baud, M. Benmalek, H. Dunlop, R. Frier and M. Jacquet, *J. Adhes.*, 1998, **65**, 307.

77 N. Ohtsu, N. Masahashi, Y. Mizukoshi and K. Wagatsuma, *Langmuir*, 2009, **25**, 11586.

78 J. W. Xu, C. H. Ha, B. Cao and W. F. Zhang, *Electrochim. Acta*, 2007, **52**, 8044.

79 B. Fang, M. S. Kim, J. H. Kim, S. Lim and J. S. Yu, *J. Mater. Chem.*, 2010, **20**, 10253.

80 P. R. Bueno and E. R. Leite, *J. Phys. Chem. B*, 2003, **107**, 8868.

81 S. W. Yang, Y. Cai, Y. W. Cheng, C.V. Varanasi and J. Liu, *J. Power Sources*, 2012, **218**, 140.

82 H. W. Bai, Z. Y. Liu and D. D. Sun, *J. Mater. Chem.*, 2012, **22**, 24552.

83 J. W. Zhang, X. X. Yan, J. W. Zhang, W. Cai, Z. S. Wu and Z. J. Zhang, *J. Power Sources*, 2012, **198**, 223.

84 P. N. Zhu, Y. Z. Wu, M. V. Reddy, A. S. Nair, B. V. R. Chowdarid and S.

Ramakrishna, *RSC Adv.*, 2012, **2**, 531.

85 H. Huang, J. W. Fang, Y. Xia, X. Y. Tao, Y. P. Gan, J. Du, W. J. Zhu and W. K. Zhang, *J. Mater. Chem. A*, 2013, **1**, 2495.

86 Z. X. Yang, G. D. Du, Z. P. Guo, X. B. Yu, Z. X. Chen, T. L. Guo and H. K. Liu, *J. Mater. Chem.*, 2011, **21**, 8591.

Tables:

Table 1 Preparation conditions of the TCNs

Sample	Precursor	PF resol (50 wt.%) (g)	TBT (g)	PF/TBT (g/g)	Citric acid (g)
TCN1	TPP1	0.93	0.24	3.88	1.00
TCN2	TPP2	0.80	0.35	2.29	1.00
TCN3	TPP3	0.65	0.43	1.51	1.00
TCN4	TPP4	0.55	0.58	0.95	1.00

Table 2 Textural properties of the TCNs

Sample	TiO_2 (wt.%)	S_{BET} ($m^2\ g^{-1}$)	V_p ($cm^3\ g^{-1}$)	V_{mes} ($cm^3\ g^{-1}$)	V_{mic} ($cm^3\ g^{-1}$)
TCN1	30.2	446	0.39	0.27	0.09
TCN2	45.3	578	0.51	0.33	0.15
TCN3	55.4	655	0.57	0.43	0.13
TCN4	68.7	385	0.26	0.16	0.06

Table 3 Comparison of the capacitive performances with other TiO_2-based composite electrodes reported previously

Samples	TiO_2 content (wt.%)	Current density (mA g^{-1})	Discharging capacity (mA h g^{-1})	Reference
TCN3	**55.4**	**34 (0.2C)** **170 (1C)**	**625 (15 cycles)** **457 (15 cycles)**	**This work**
quasi-3DOM TiO_2	100	25 250	195 (5 cycles) 121 (5 cycles)	[54]
3DOMM TiO_2	100	33.6 (0.2C) 168 (1C)	236 (5 cycles) 175 (5 cycles)	[55]
C-TiO_2 nanosheets	89	170 (1C)	186 (15 cycles)	[24]
Mesoporous TiO_2-C nanospheres	94	34 (0.2C)	163 (15 cycles)	[25]
C-TiO_2 mesoporous spheres	74	66	250 (30 cycles)	[26]
Mesoporous TiO_2/C nanofibers	86.2	170 (1C)	122 (15 cycles)	[27]
TiO_2 nanorods/RGO	81	168 (1C)	190 (5 cycles)	[33]
C/TiO_2+C spheres	54.07	170 (1C)	161 (5 cycles)	[82]
TiO_2/C composite nanotubes	95	1C	220 (cycles)	[83]
TiO_2-CNT	92	150	153 (cycles)	[84]
OMC-TiO_2	65	35 (0.1C) 175 (0.5C)	550 (15 cycles) 299(15 cycles)	[29]
Graphene-TiO_2(B) hybrid	66.3	150	430 (10 cycles)	[85]
TiO_2(B)@C nanowires	63.33	30	705 (10 cycles)	[86]

Figure captions:

Fig. 1 Typical SEM images of the PS template (a), TCN1 (b), TCN2 (c), TCN3 (d), and TCN4 (e); energy-dispersive X-ray analysis on the TCN3 in an elemental mapping mode (f).

Fig. 2 Wide-angle XRD patterns of the TCNs.

Fig. 3 N_2 sorption isotherms (left) and corresponding pore size distributions (right) of the TCNs.

Fig. 4 Representative TEM images of the TCN3 at low-magnification (a) and high-magnification (b), high-resolution TEM image of the TCN3 wall (c).

Fig. 5 XPS spectra of Ti 2p of the TCNs.

Fig. 6 Charge/discharge curves of the TCNs at the current density of 0.2 C.

Fig. 7 Nyquist plots of impedance data for the TCNs in the frequency range from 100 kHz to 10 mHz.

Fig. 8 Capacity *vs.* cycle number curves and coulombic efficiencies of the TCN electrodes from the first cycle to the 100th cycle at the current density of 0.2C.

Fig. 9 Rate capability of the TCN3 electrode as a function of current density from 0.2C to 10C (a), SEM image of the TCN3 electrode after completing 100 charge/discharge cycles (b).

Fig. 10 Proposed diagram for lithium ions diffusion and insertion into the TCN.

Figures:

Fig. 1

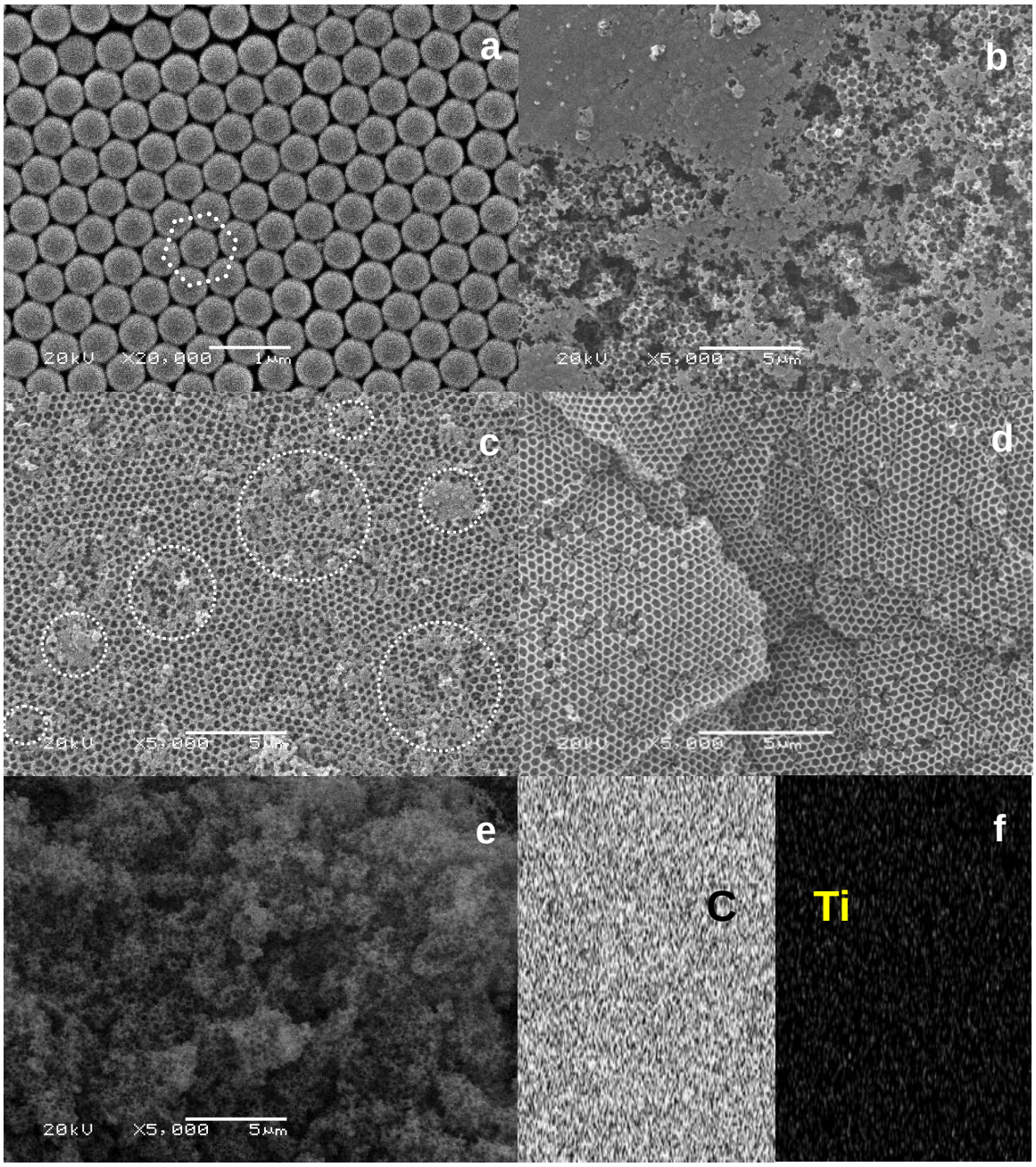

Fig. 2

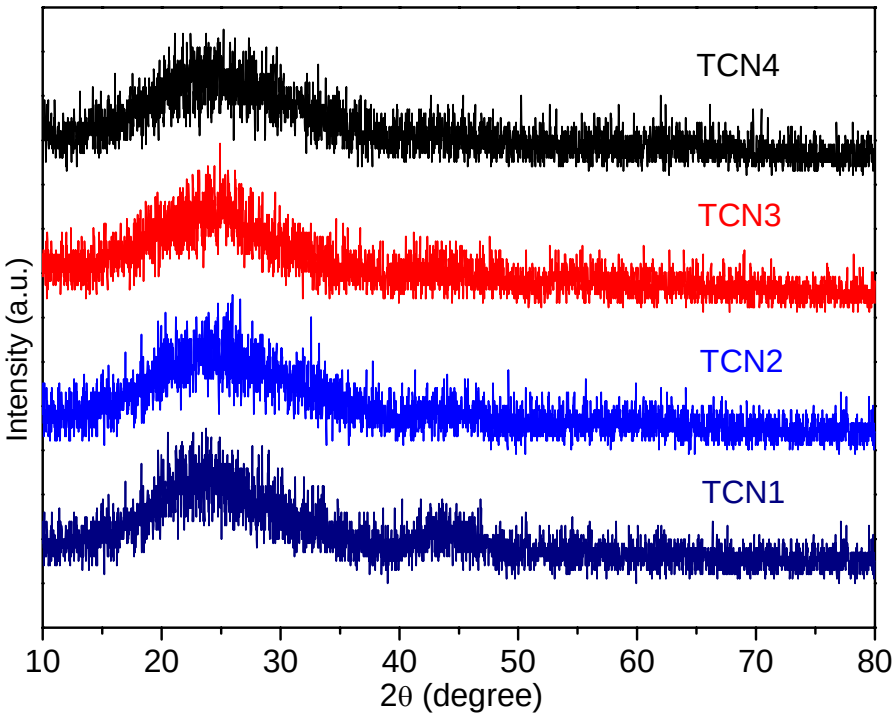

Fig. 3

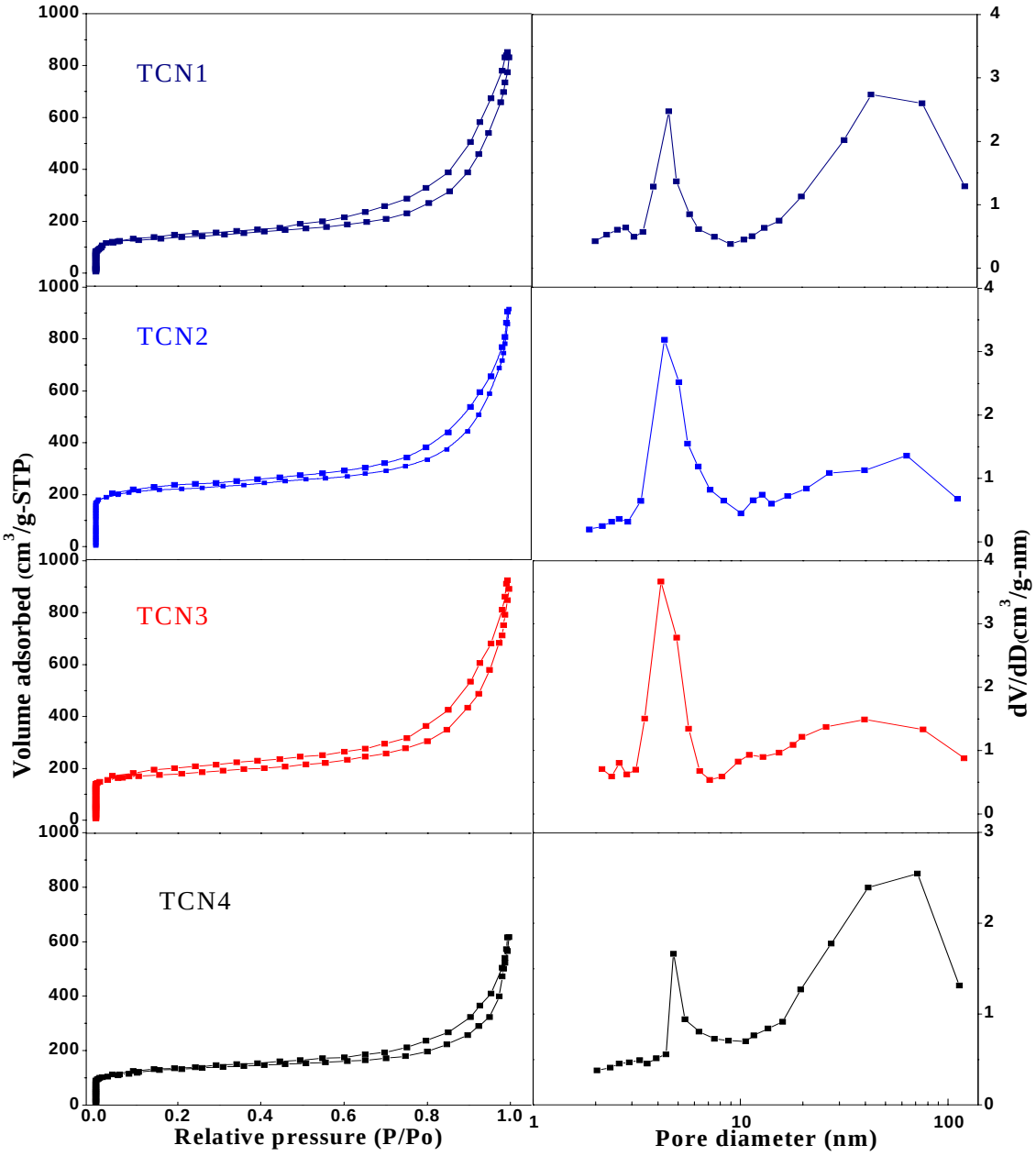

Fig. 4

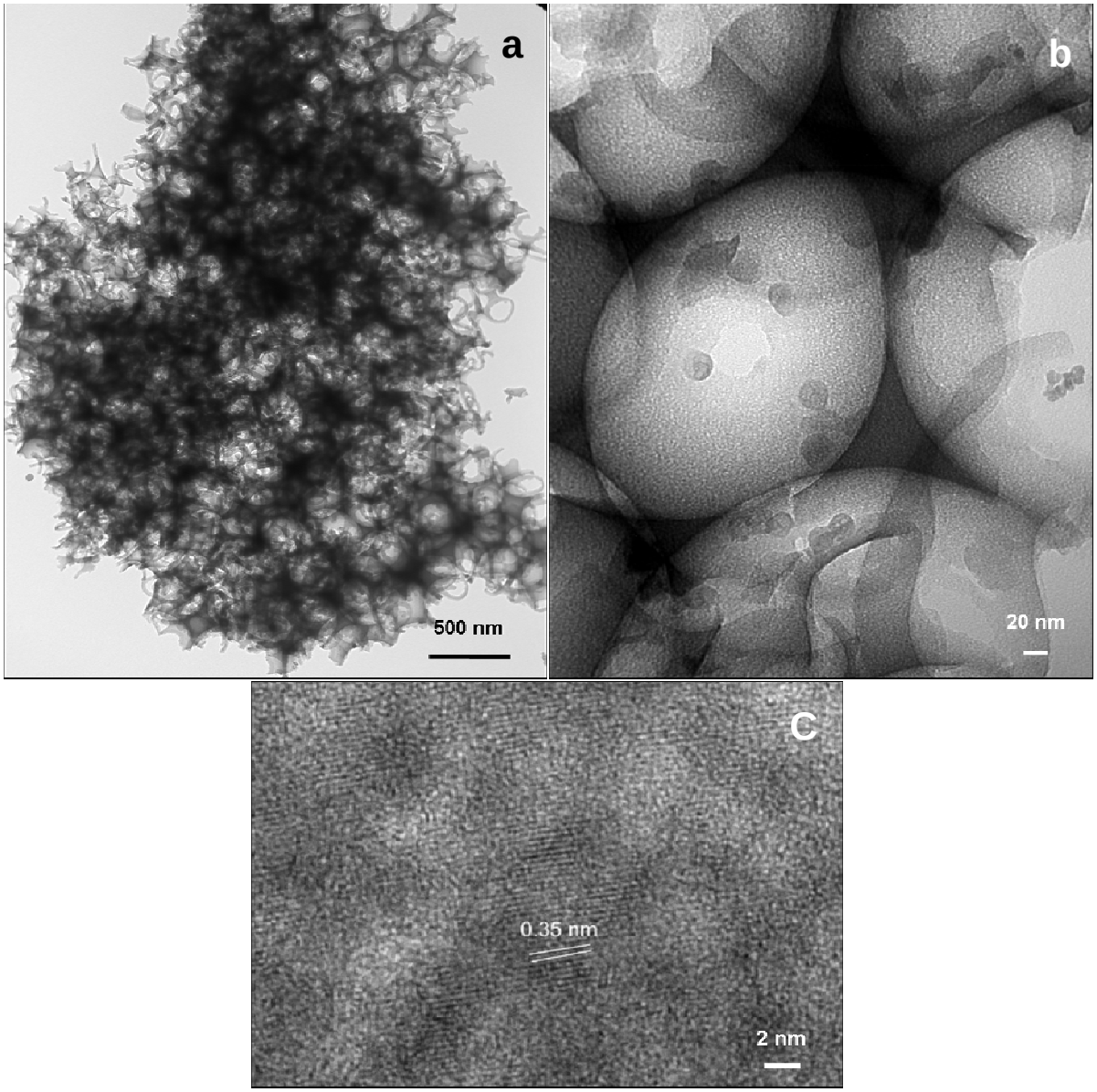

Fig. 5

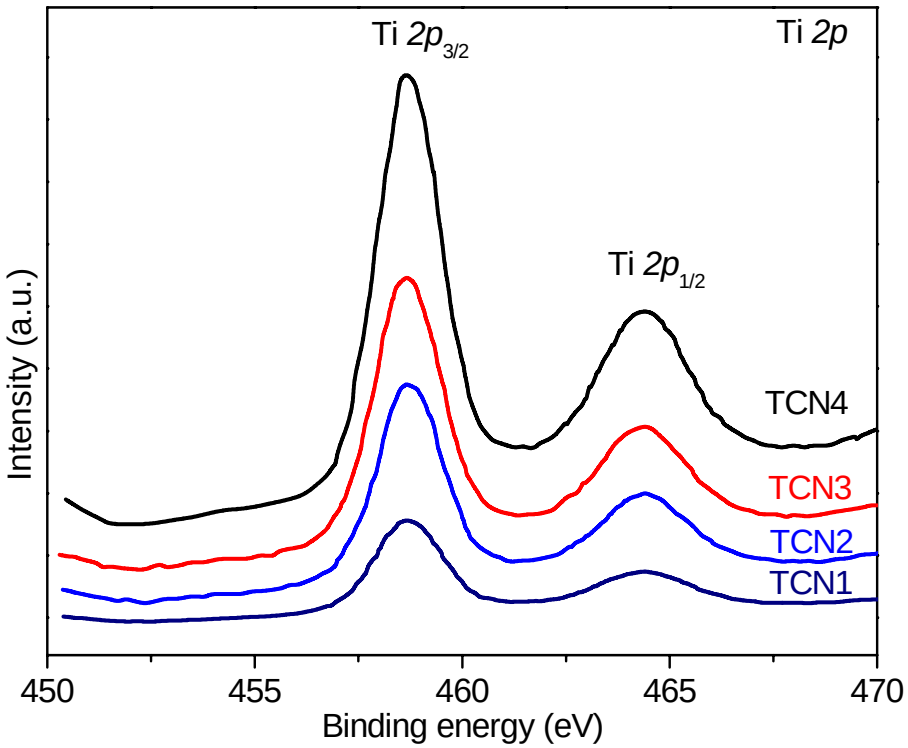

Fig. 6

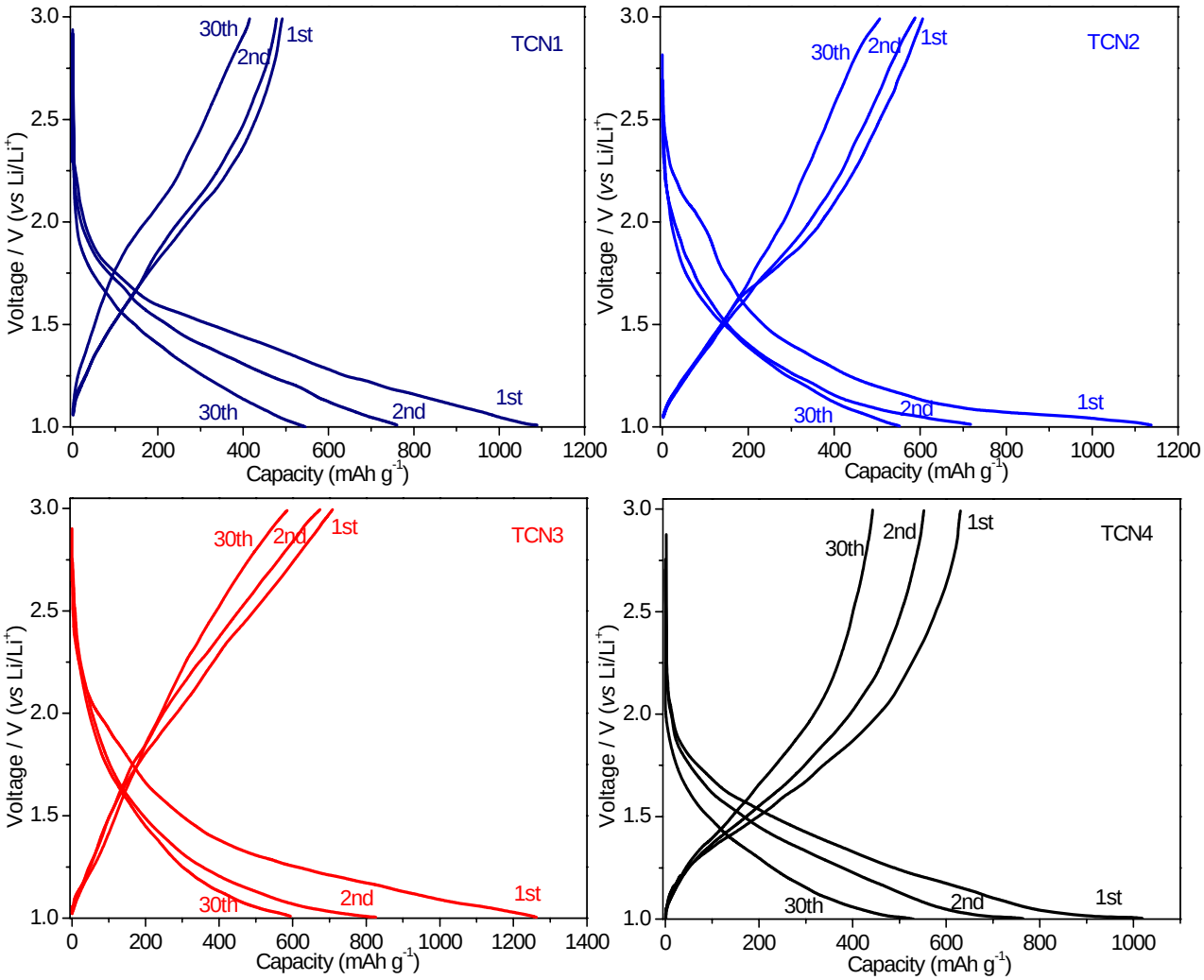

Fig. 7

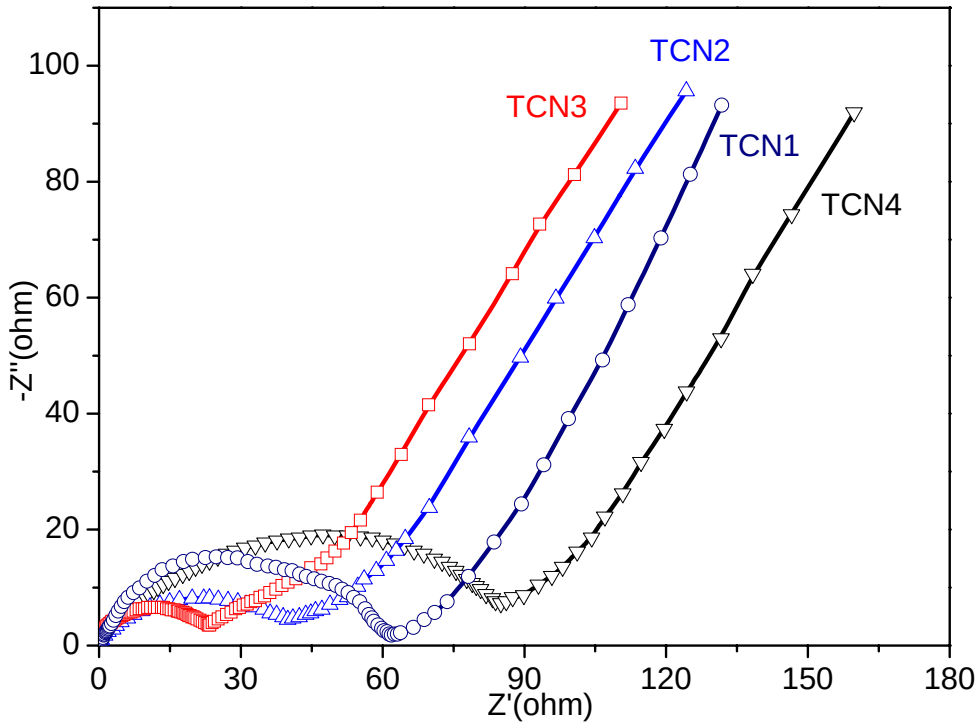

Fig. 8

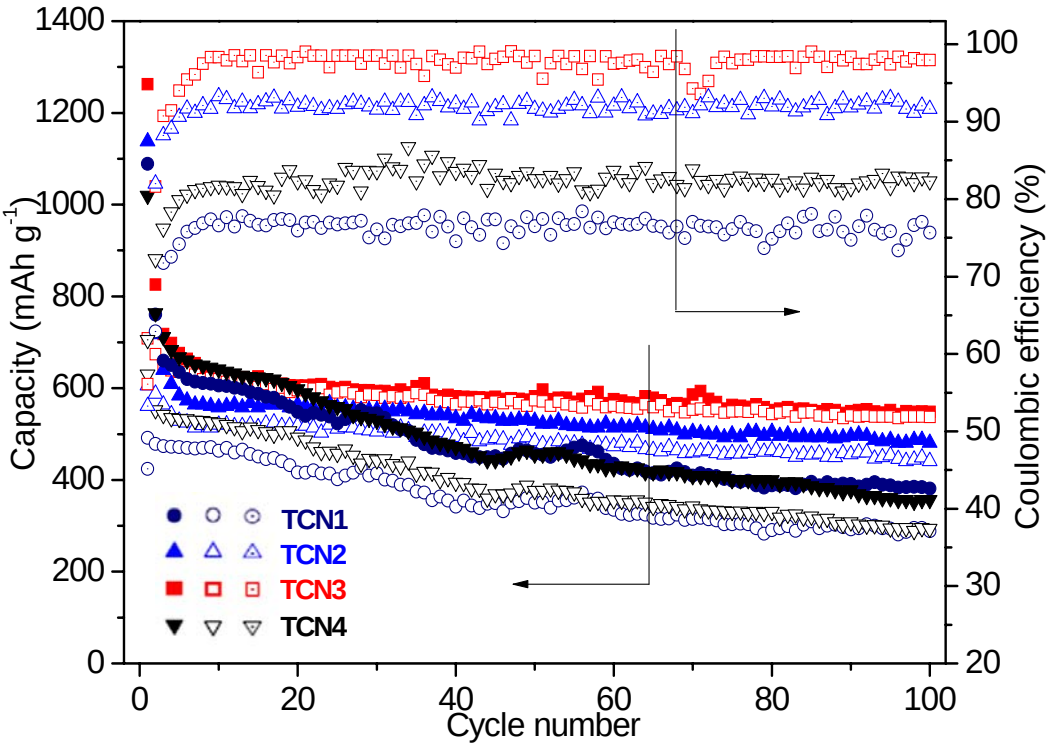

Fig. 9

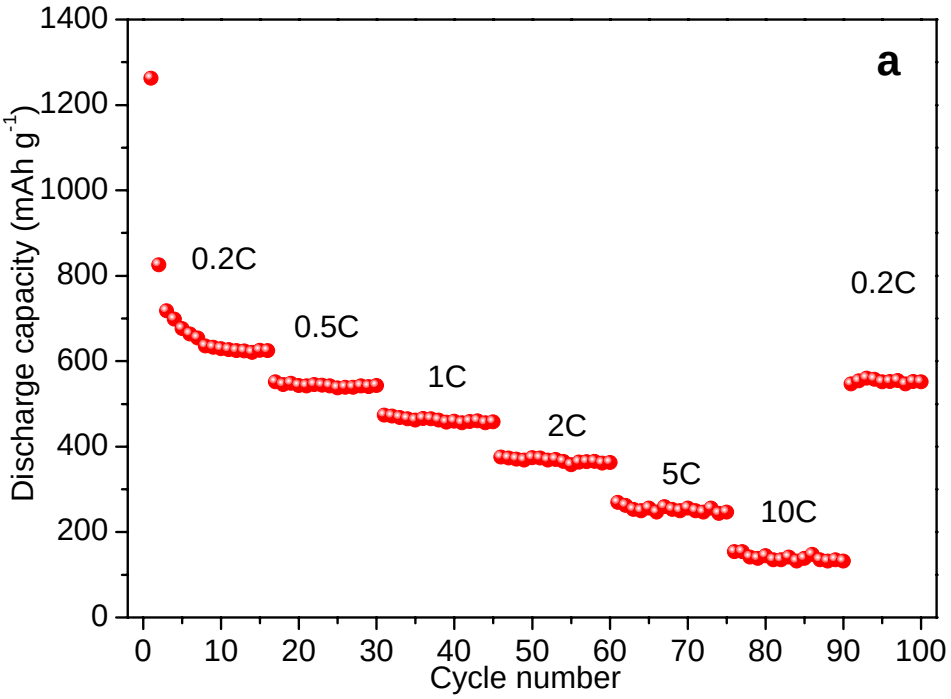

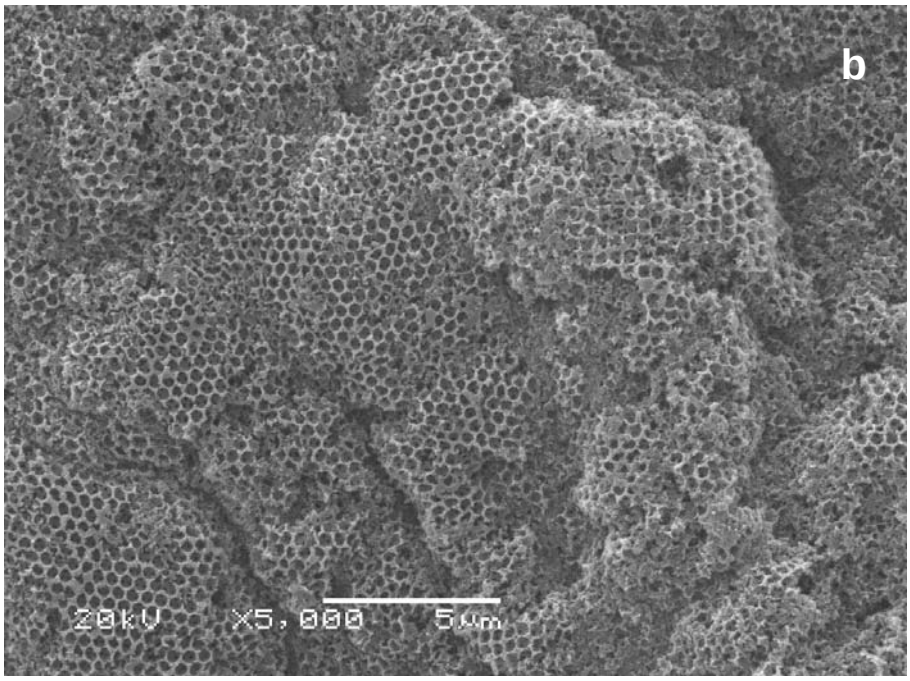

Fig. 10

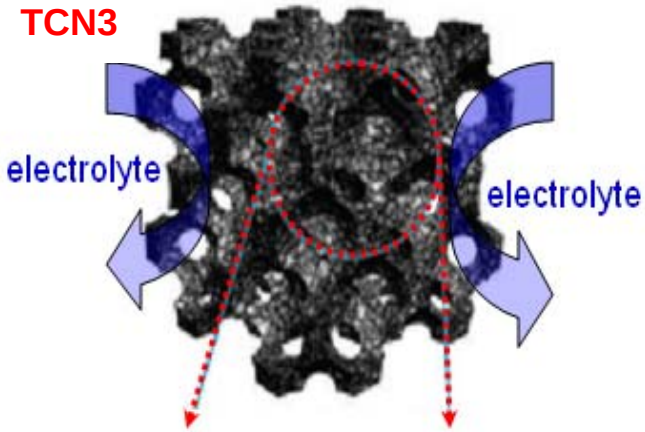

$6C + xLi^+ + xe^- \longleftrightarrow LixC_6$

$TiO_2 + yLi^+ + ye^- \longleftrightarrow LiyTiO_2$